Title

Intra-individual Physiomic Landscape of Pyramidal Neurons in the Human Neocortex

Authors

Henrike Planert[1]*, Franz. X. Mittermaier[1]*, Sabine Grosser[2]*, Pawel Fidzinski[3,7], Ulf C. Schneider[5], Helena Radbruch[4], Julia Onken[5], Martin Holtkamp[3], Dietmar Schmitz[6,7], Henrik Alle[1], Imre Vida[2#], Jörg R.P. Geiger[1#] & Yangfan Peng[1,3#]

*Equal contribution
#Joint supervision
[1]Institute of Neurophysiology, [2]Institute for Integrative Neuroanatomy, [3]Department of Neurology, [4]Department of Neuropathology, [5]Department of Neurosurgery, [6]Neuroscience Research Center, [7]NeuroCure Cluster of Excellence, Charité - Universitätsmedizin Berlin, Corporate Member of Freie Universität Berlin and Humboldt Universität zu Berlin.

Abstract

Computation within cortical microcircuits is determined by functional properties of the neurons and their synaptic interactions. While heterogeneity of inhibitory interneurons is well established, the anatomical, physiological, and molecular differentiation of excitatory pyramidal neurons is not fully resolved. To identify functional subtypes within the pyramidal neuron population, we focused on human layer 2-3 cortex which greatly expanded during evolution. We performed multi-neuron patch-clamp recordings in brain slices from the temporal cortex of 22 epilepsy patients. We characterized the electrophysiological properties of up to 80 pyramidal neurons per patient, enabling us to assess inter- and intra-individual functional variability. Hierarchical clustering of the high-dimensional parameter space yielded functionally distinct clusters of pyramidal neurons which were present across individuals. This may represent a generic organizational principle converging with previously described transcriptomic heterogeneity. We further observed substantial heterogeneity in physiological parameters with intra-individual variability being severalfold larger than inter-individual variability. The phenotypic variability within and across pyramidal neuron subtypes has important implications for the computational capacity of the cortical microcircuit.

Introduction

The function of the brain emerges through interaction of diverse neuron types. The identity and characteristics of these neuron types have been subject of intense study since the seminal work by Ramón y Cajal (*1*). To better understand the functional role of neuronal diversity, classifications have been made based on single-cell physiology, anatomy and molecular markers. Initial studies described a largely homogeneous pyramidal neuron population in contrast to distinct interneuron types, underestimating their diversity beyond layer- and projection-specific subtypes (*2-4*). More recently, high-throughput molecular approaches led to detailed cortical taxonomies, including human neurons, based on their common gene expression (*5-11*). Efforts to map these transcriptomic types (t-types) to their morpho-electrical properties revealed both discrete and continuous phenotypic variation between t-types (*5, 6, 12*). This highlights the ongoing challenge to identify discrete entities of neuronal subtypes based on their molecular, morphological, and physiological profile (*13*).

Neuronal cell classes appear broadly conserved across species (*7, 8, 14*) . Nevertheless, functional specialization of the human cortex has been proposed, although the cellular and circuit implementation for this is not well understood (*15*). Especially human cortical layers two and three (L2-3) expanded during evolution (*16, 17*), and its pyramidal neurons possess unique morphology, cortical depth-dependent electrophysiology, as well as distinct dendritic computations (*18-22*). Anatomically, two pyramidal neuron subtypes were identified based on different dendritic morphologies (*23*). Transcriptomic studies of human L2-3 found an increased pyramidal neuron diversity, corresponding to five types that diverged with respect to their electrophysiological and morphological characteristics (*5, 8*). While a subtype classification based on electrophysiology (e-types) in human layer 5 (L5) was able to distinguish between transcriptomically defined extra-telencephalic and intra-telencephalic projecting neurons (*24*), the granularity of functional pyramidal neuron subtypes in the human L2-3 remains to be resolved.

Functional classification of pyramidal neuron subtypes might be challenging due to multiple confounding factors, such as differences between areas and individuals. Comparative studies across regions suggest variations of neuron properties across the cortical sheet (*10, 25*). Furthermore, substantial inter-individual variability of neurons has been observed across species, including crabs, mice and humans (*25-27*). In order to assess the diversity of human L2-3 pyramidal neurons and to disentangle the effects of inter-individual variability, we characterized functional properties in large samples of neurons from individual patients. We performed multi-neuron patch-clamp recordings on human brain slices from temporal cortex of epilepsy patients (*28*) and identified distinct functional subtypes which were present across individual patients. While we identified inter-individual differences, we found that intra-individual variability was several folds higher.

Results

High yield intrinsic and synaptic recordings per single patient make individualized analysis possible. We used resected cortical tissue from 22 patients diagnosed with refractory epilepsy and undergoing temporal lobe surgery (10 females and 12 males, age range from 21 to 55 years; Fig. 1A, suppl. Table 1). In order to maximize experimental yield per patient at high recording quality, we established specialized recording setups and procedures. These included sterile slicing conditions and parallel recording on two optimized multi-patch setups employing reuse of individual pipettes (*28*). Up to ten neurons in cortical L2-3 were recorded simultaneously (Fig. 1B-D). Out of 1429 recorded neurons, 964 met our inclusion criteria and were classified as pyramidal neurons based on their electrophysiological properties (see method section). The neurons were filled with biocytin and subsequently visualized (Fig. 1C). Up to 80 pyramidal neurons per patient and their respective

monosynaptic connections were recorded, making analysis on the single patient level possible (Fig. 1E).

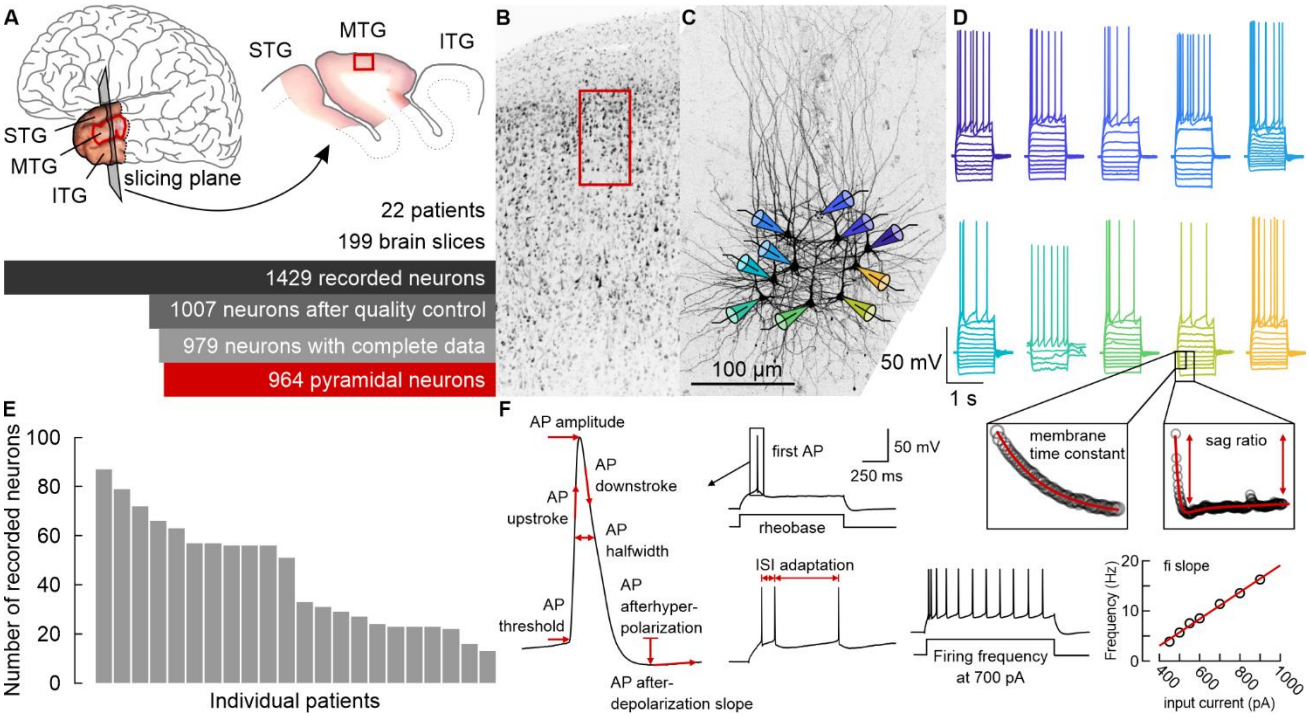

Figure 1: High throughput whole-cell patch-clamp recordings per single patient. (A) Human cortical brain tissue was obtained from patients that underwent surgery for temporal-lobe epilepsy. A typical specimen consisting of the temporal pole and anterior parts of the superior, medial and inferior temporal gyrus (STG, MTG and ITG, respectively) is shown in relation to the entire human cerebrum. In total, 199 acute cortical slices from tissue of 22 patients were measured. Of 1429 recorded neurons, 964 passed quality control, had complete data and were classified as pyramidal neurons. **(B)** Nissl staining of cortex, red inset highlights L2-3 where most recordings were performed. **(C)** Biocytin staining of recorded neighbouring neurons. Colored patch pipettes depict multi-neuron patch-clamp approach, one neuron was not stained (dashed circle). **(D)** Voltage responses of the neurons in panel B with the respective colored pipette are shown for a sequence of increasing step current injections (50-100 pA increments). **(E)** Bar plot showing number of recorded neurons with complete data per patient, sorted in a descending order. **(F)** Schematics depicting the electrophysiological parameters extracted from the raw traces by an automated analysis pipeline. For this study 15 well established electrophysiological properties were analysed (see Methods).

Human L2-3 pyramidal neurons are functionally heterogenous and occupy a high-dimensional parameter space. We extracted 15 active and passive electrophysiological properties, similarly to previous studies addressing the functional phenotype of neurons (Fig. 1F, (*12, 21, 29*). The pyramidal neurons were highly diverse with respect to their electrophysiological properties, showing broad and in some cases skewed distributions (Fig. 2A, Table 1). Some properties were strongly correlated, such as broader action potential (AP) halfwidths with slower AP downstrokes (R = -0.8), higher firing frequency with higher input resistances (R = 0.56) or larger AP amplitudes with faster AP upstroke (R = 0.69, Fig. 2C). In order to quantify the overall degree of correlation between functional parameters, we conducted a principal component analysis. The first principal component explained 24% of the total variance in the dataset, and the top three components amounted to 52% percent (Fig. 2D). Thus, while some degree of correlation was identified between properties, the overall functional parameter space of the pyramidal neurons appears to be rather high-dimensional.

Electrophysiological parameter	Unit	Median	Interquartile range		Skewness
Resting membrane potential	mV	-73.4	-77.7	-69.4	0.1
Input resistance	MΩ	74.0	50.4	108.4	2.2
Membrane time constant tau	ms	18.5	15.7	21.8	0.8
AP threshold amplitude	mV	-37.2	-40.6	-34.1	0.0
AP amplitude	mV	84.5	78.8	89.7	-0.3
AP halfwidth	ms	0.86	0.75	1.00	0.5
AP upstroke	mV/ms	361	307	425	0.6
AP downstroke	mV/ms	84.6	72.0	97.0	6.4
AP afterhyperpolarization	mV	14.3	12.3	16.6	0.7
AP afterdepolarization slope	mV/ms	0.30	0.06	0.62	1.4
Interspike interval adaptation index	ratio	2.07	1.56	3.22	5.3
Frequency at 700 pA	Hz	22.0	15.0	30.0	6.8
Sag ratio	ratio	1.08	1.03	1.14	1.2
Rheobase	pA	250	200	350	0.6
fi slope	Hz/pA	0.04	0.03	0.05	7.2

Table 1: Descriptive statistics of the 15 electrophysiological parameters.

Human L2-3 pyramidal neurons can be classified into distinct functional subtypes. To disambiguate whether the heterogeneous pyramidal neurons occupy a continuum in the high-dimensional space or are grouped in sub-spaces, we performed an unsupervised hierarchical cluster analysis. Based on a Monte Carlo approach for testing statistical significance of the clustering (*21, 30*), we identified five electrophysiologically distinct subtypes (e-types) of pyramidal neurons in our high dimensional dataset (Fig. 2E). To better understand their functional properties, we performed Random Forest Feature Importance analysis to highlight the most distinguishing parameter for each e-type (Fig. 2G). Most notably, e-type 3 (green) exhibits a high inter-spike interval adaptation, reflecting initial doublet spiking. In addition, e-type 2 (blue) is characterized by a prominent voltage sag in comparison to other types (Fig. 2G). We visualized this high-dimensional parameter space using Uniform Manifold Approximation and Projection (UMAP, see Methods). This revealed functional clusters with broad distributions and regions of overlap (Fig. 2F). However, as these results are generated from pooled data of 22 patients, it remains an open question to what extend this functional heterogeneity is determined by inter-individual differences or whether it represents a generic pattern across individuals.

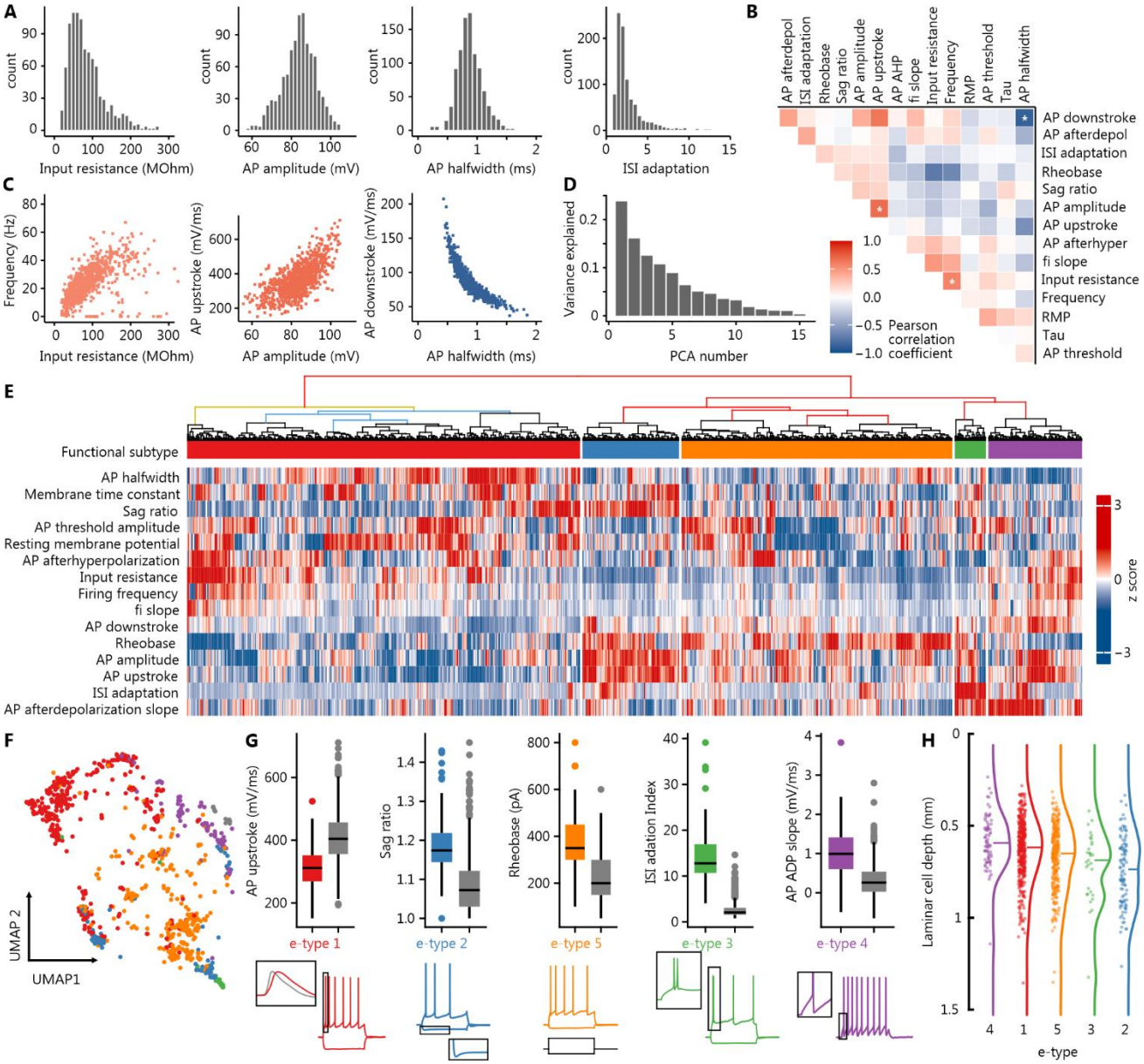

Figure 2: High-dimensional functional heterogeneity of L2-3 pyramidal neurons. (A) Histograms show distributions of example electrophysiological parameters. **(B)** Matrix shows Pearson correlation coefficient for each pair of parameters. **(C)** The parameter pairs with strong correlation as highlighted by asterisks in (B) are shown as scatter plots. The color of data points reflects the Pearson correlation coefficient. **(D)** A Scree plot of a principal component analysis of the 15 electrophysiological properties shows the variance explained by each principal component. The fact that the top 3 principal components explain only 52% of the variance suggests that the parameter space is rather high-dimensional. **(E)** A clustergramm visualization of the electrophysiological parameters for all 964 pyramidal neurons, grouped according to the hierarchical clustering based on Ward's method. The colours in the dendrogram on top indicate the results of the statistical testing of the bifurcations ('sigclust2' R package, see Methods): Red indicates significant bifurcations (p-values < 0.021, corrected for family wise error), yellow indicates non-significant bifurcations, blue indicates untested bifurcations due to non-significant bifurcation above, and black indicates untested bifurcations due to cluster size below threshold. Each column represents one neuron, and the color code represents the z-score of each parameter (rows). Five functional clusters were identified (e-types, see Methods) and are shown by the color code in the top row. **(F)** Uniform Manifold Approximation and Projection (UMAP) dimensionality reduction was performed to visualize the high-dimensional parameter space. Each dot represents one neuron positioned according to its set of parameters and color coded by the membership in one of the e-types as determined by the hierarchical clustering. **(G)** The most distinguishing parameter of each e-type is shown. The boxplots illustrate the comparison between the neurons of a respective e-type (color code) with all other neurons (grey) for a given parameter. Below are example traces shown for each e-type with insets highlighting the most distinguishing property. **(H)** Laminar cell depth position is shown for each pyramidal neuron, color-coded and grouped by the e-type. E-types are sorted based on descending medians. Note that group 4 seems to be restricted to superficial layers, whereas the doublet spiking group (e-type 3) appears distributed across cortical layers.

E-types of human L2-3 pyramidal neurons are found across individuals. To characterize inter-individual variability, we compared the clustering result of pyramidal neurons at the level of single

patients. Individualized UMAPs showed a high degree of similarity across patients with respect to patterns of distribution (Fig. 3B). Additionally, we assessed the fraction of e-types in patients with more than 50 sampled neurons and found that all e-types were present in each individual, with exception of the least common e-type being absent in 3 patients (Fig. 3C). While the relative proportions of e-types differed in each patient, they largely resemble the overall fractions. Thus, our analysis of the high-dimensional parameter space showed preserved e-types across individuals, suggesting a functionally relevant subdivision of pyramidal neurons.

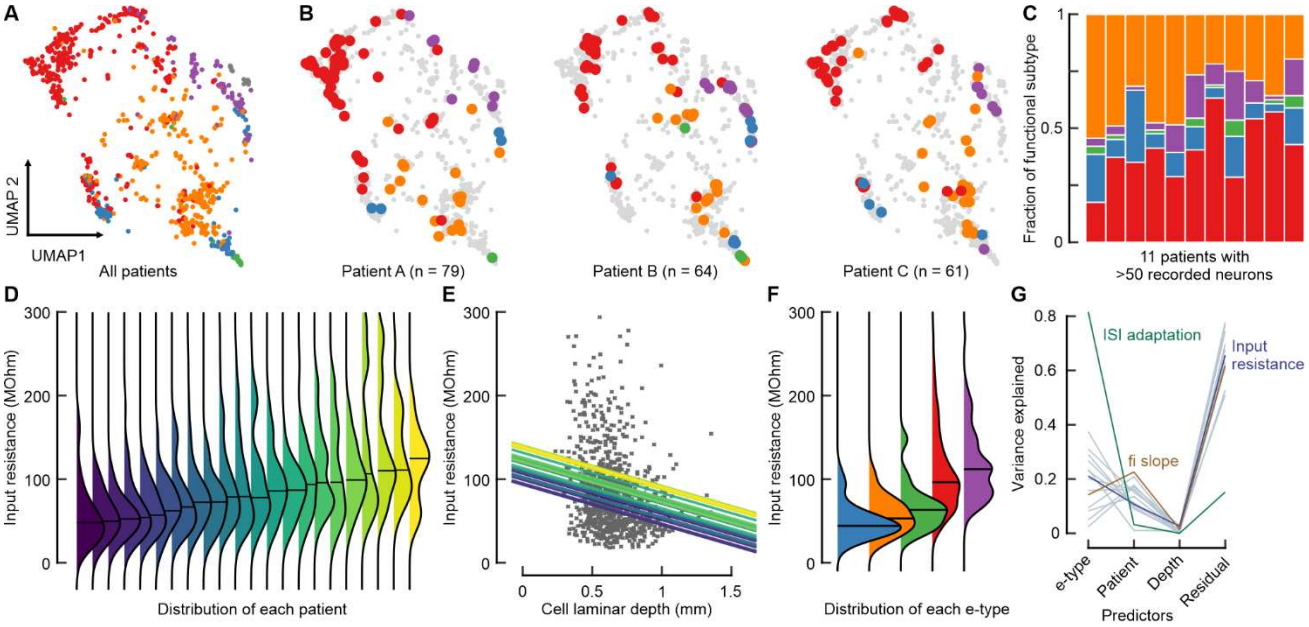

Figure 3: Inter-individual comparison of functional heterogeneity. (A-B) UMAP visualization of neurons from all patients (A) and of neurons only from individual patients with large sample sizes (B). The color of the data points corresponds to the e-type of the respective neurons (red = e-type 1, blue = e-type 2, green = e-type 3, purple = e-type 4 and orange = e-type 5). Note that the patient specific UMAPs show a high degree of similarity. **(C)** Stacked bar plots show relative fraction of different e-types for 11 patients, in which more than 50 pyramidal neurons were recorded. **(D)** Smoothed distributions of input resistance are shown for each patient, sorted by ascending patient medians (each patient is represented by a different color). **(E)** Scatter plot shows the distribution of input resistance across the cortical depth (each grey dot represents a recorded pyramidal neuron). The colored lines represent the patient-specific intercepts and the fixed slope approximated by the linear mixed-effects model. **(F)** Smoothed distributions of input resistance are shown for the different e-types. **(G)** Line plot indicates the relative contribution of the predictors to the explained variance of each electrophysiological parameter Each line represents one parameter with three selected parameters highlighted in color.

Intra-individual functional variability is severalfold larger than inter-individual variability. To assess the contribution of inter-individual differences to the functional heterogeneity, we compared the distributions of single parameters across patients. While we observed small differences in medians between patients, the distributions for individual patients were broad and overlapping (Fig. 3D), suggesting small inter-individual vs. large intra-individual variability (Input resistance: SD of individual means = 25 MΩ, mean intra-individual SD = 47 MΩ). To further quantify to what extent the heterogeneity of physiological parameters is determined by inter-individual differences and other factors, such as the identified e-types and the localization of the neuron relative to pia, we fit linear mixed-effects models to the data (Fig. 3E, see Methods). We compared the relative contribution of these three predictors to the total variability of each parameter (Fig. 3G, Table 2). On average, the model attributed about 13% of total variability to differences between patient samples. For example, inter-individual differences were responsible for 11% of input resistance variability. In general, e-types accounted for a larger proportion of variability (interquartile range: 19-29%). Notably, variability of ISI adaptation was explained to a high degree through e-types (78%). This is likely due to the fact, that e-type 3 (doublet spiker) is characterized by a markedly larger ISI adaptation than other types. The dependence of physiological parameters on cortical depth has been described previously (*5, 22, 31*). We found that the distance of the pyramidal neuron soma to the pial surface had a significant effect

on most parameters, such as input resistance (Fig. 3E), sag ratio, fi-slope, AP ADP slope, AP frequency, and AP up- and downstroke (Table 2). However, the explained variability by depth is relatively small compared to the other predictors (Fig. 3G, Table 2). The residual, unexplained, variability within the individual patients for all parameters, except for ISI adaptation, remains high (interquartile range 57-68%). This demonstrates that within-individual variability is about five times higher than that between individuals.

		Variance explained in LME model					
Electrophysiological parameter	**Unit**	**Cell depth**	**Inter-individual**	**e-type**	**Residual**	**Fixed slope unit/mm**	**p-value of fixed effect**
Resting membrane potential	mV	0.0%	17%	26%	57%	-0.23	0.835
Input resistance	MΩ	2.7%	11%	19%	67%	-47.97	0.000
Membrane time constant	ms	0.6%	13%	10%	77%	2.26	0.023
AP threshold amplitude	mV	0.3%	14%	35%	51%	-1.99	0.038
AP amplitude	mV	0.3%	12%	20%	68%	2.6	0.086
AP halfwidth	ms	0.7%	16%	19%	65%	0.1	0.007
AP upstroke	mV/ms	1.0%	10%	32%	57%	49.29	0.001
AP downstroke	mV/ms	1.4%	10%	25%	64%	-13.24	0.000
AP afterhyperpolarization	mV	0.2%	14%	22%	64%	-0.97	0.129
AP afterdepolarization slope	mV/ms	3.0%	16%	26%	54%	-0.5	0.000
Interspike interval adaptation	ratio	0.0%	4%	78%	19%	0.07	0.884
Frequency at 700 pA	Hz	1.5%	23%	13%	63%	-7.95	0.000
Sag ratio	ratio	1.1%	1%	19%	79%	0.05	0.001
Rheobase	pA	0.2%	9%	31%	59%	27.62	0.143
fi slope	Hz/pA	2.9%	17%	2%	78%	-0.02	0.000

Table 2: Results of linear mixed-effect models. Relative proportions of variance explained are shown for the three predictors cell depth, patient identity and e-type, and the residual. The fixed slope approximates the linear dependence of the electrophysiological parameter on the cortical depth, e.g. the input resistance decreases by 48 MΩ per mm cortical depth. The statistical significance of this linear fit is indicated by the p-value.

Discussion

By recording a large number of pyramidal neurons within L2-3 human temporal cortex, we were able to characterize the functional landscape of this population in a higher granularity than previous studies in rodents and humans (*12, 21-23, 31, 32*). This allowed us to identify electrophysiological subtypes (e-types) that exhibited distinct functional properties. While previous studies in rodents and monkeys described electrophysiological subtypes of L2-3 pyramidal neurons (*33, 34*) that could relate to different projection targets (*35*), the functional heterogeneity in human L2-3 pyramidal neurons has mostly been attributed to a continuous gradient along the cortical depth (*21, 22, 31*). In contrast, human L5 pyramidal neurons have been shown to comprise three distinct e-types (*24*). In our study of human L2-3, the statistical significance of our hierarchical clustering argues for a separation of pyramidal neurons into at least five e-types rather than a continuous variation of physiological parameters. While we could also confirm a significant dependence of certain functional parameters on the cortical depth, the linear mixed-effects models, applied here, attributed only up to 3% of explained variance to this predictor. This finding argues for a large functional heterogeneity of these neurons which exists independent of the soma location.

Recent studies described a large transcriptomic diversity which implicates differential expression of proteins that determine the phenotypic properties of individual neurons (*12*). For human L2-3 pyramidal neurons, several different t-types have been proposed (*5, 8, 36*). While they exhibit

divergent physiological properties, a classification based on physiology alone was only able to predict the t-type of superficial L2-3 pyramidal neurons with 49% accuracy (*5*). In line with this, the properties of the e-types, identified in this study, do not seem to directly correspond to the properties of the t-types in those studies. This fact further highlights large phenotypic variability within and across t-types (*12*), indicating substantial translational and posttranslational regulation in neurons which may reflect adaptation to specific functional and computational requirements. In accordance, recent theoretical studies have shown that heterogeneity in single neuron parameters represents a critical source of functional specialization as well as robust encoding and learning in cortical microcircuits (*37-39*).

Inter-individual differences of electrophysiological properties of neurons have been reported in entorhinal cortex in the mouse and in the stomatogastric ganglion in the crab (*26, 40*). These may reflect different solutions to generate an adaptive higher-order circuit performance. In human neurophysiology studies, the genetic and environmental background are usually uncontrolled although they represent important confounding factors. We find that electrophysiological properties exhibit different degree of variability due to inter-individual differences. Specifically, we identified parameters with substantial inter-individual variability, such as firing frequency or AP halfwidth. This may motivate future studies to reveal the contribution of these parameters to different circuit-level computation across individuals. Accordingly, initial investigations have associated AP kinetics in L2-3 with higher cognitive function (*41*). Additionally, increased sag ratio in L5 was observed with higher age (*42*). However, we identify over 80% of variability attributed to sources independent of inter-individual differences, suggesting that single neuron properties are substantially tuned for functional specialization within their respective microcircuit at the level of the individual. This emphasizes that large sample sizes from individual patients are needed to identify valid associations between single neuron properties and patient characteristics.

Methods

Human Subjects

The data obtained in this study was measured in acute brain slices obtained from temporal lobe resections in 22 patients suffering from pharmacologically refractory epilepsy (12 male, 10 female, age range 21 to 55 years with median age of 34 years). The study procedures adhered to ethical requirements and were approved by the local ethical committee with Approval Nr. EA2/111/14. Prior written informed consent for the scientific use of resected tissue was given by the patients.

Patient	Gender	Age (year)
1	m	36
2	f	45
3	f	55
4	m	40
5	m	27
6	m	30
7	f	21
8	m	22
9	m	35
10	f	21
11	f	48
12	m	36
13	f	22
14	f	36
15	f	34
16	m	34
17	m	31
18	f	27
19	m	48
20	m	32
21	f	25
22	m	53

Supplementary table 1: Patient metadata

Experimental procedures

Human Brain Slice Preparation

Temporal lobe pole tissue resected from the patients was transferred from the operating theatre to the laboratory in sterile and cooled sucrose-based aCSF (in mM: 87 NaCl, 2.5 KCl, 3 $MgCl_2$, 0.5 $CaCl_2$, 10 glucose, 75 sucrose, 1.25 NaH_2PO_4, and 25 $NaHCO_3$, 310 mOsm) enriched with carbogen (95% O2, 5% CO2) within 15-40 min after resection. The pia mater was removed from the surface and the tissue was cut under sterile conditions in ice-cold sucrose-based aCSF to 300 or 400 µm-thick slices. After a 30 minutes recovery period at 34°C, slices were held submerged at room temperature in sucrose-based aCSF. In a subset of experiments, an antibiotic (Minocycline, 2 µM) was added to the incubation solution. Recordings were made up to 52 hours after slicing (interquartile range: 7.5-26 hours).

Patch-Clamp Recordings

Slices were transferred to the recording chambers of two patch-clamp setups optimized for high-throughput microcircuit assessment of rare tissue samples, including automated pipette pressure and

pipette cleaning systems (*28*). The eight-manipulator setup included the following equipment: Eight PatchStar manipulators (Scientifica), BX-51 WI microscope (Olympus), Orca-Flash 4.0 LT Camera (Hamamatsu), MultiClamp 700B amplifiers (Molecular Devices), Digidata 1550 digitizer (Molecular Devices). The ten-manipulator setup included ten u-Mp micromanipulators (Sensapex), Eclipse FN1 microscope (Nikon), Orca-Flash 4.0 LT Camera (Hamamatsu), MultiClamp700B amplifier (Molecular Devices), Power1401-3A digitizer (Cambridge Electronic Design). Data were low-pass filtered with Bessel filter at 6 kHz and digitized at a sampling rate of 20 kHz. Data acquisition was performed using pClamp 10 (Molecular Devices) or Signal 6 acquisition software (Cambridge Electronic Design).

Patch pipettes were pulled from borosilicate glass capillaries (2 mm outer/1 mm inner diameter; Hilgenberg) on a horizontal puller (P-97, Sutter Instrument Company). They were filled with K-gluconate based intracellular solution containing (in mM) 130 K-gluconate, 2 $MgCl_2$, 0.2 EGTA, 10 Na_2-phosphocreatine, 2 Na_2ATP, 0.5 Na_2GTP, 10 HEPES buffer and 0.1% biocytin (290– 295 mOsm, pH adjusted to 7.2 with KOH) and had 5-8 MΩ resistance. The liquid junction potential was calculated to be 16 mV and was not corrected for. Neurons were visualized using the differential interference contrast infrared microscope and pyramidal neuron-like soma were selected. Whole-cell patch-clamp recordings of these L2-3 neurons were performed at 34℃ under submerged conditions, with continuous perfusion of aCSF containing (in mM) 125 NaCl, 2.5 KCl, 1 $MgCl_2$, 2 $CaCl_2$, 10 glucose, 1.25 NaH_2PO_4, and 25 $NaHCO_3$ (300 mOsm). Pipette access resistance and capacitance were compensated throughout the experiment, and remaining effects of these were addressed offline by means of reverse RC filtering (see quality control and de-filtering procedure below). For the assessment of electrophysiological properties, we applied a range of step currents in current clamp mode (see intrinsic physiology feature analysis below) within the initial 30 minutes of recording.

Morphology

After recording, slices were fixed overnight in a fixative solution containing 4% paraformaldehyde with 0.1 M Phosphate buffer (PB, pH 7.4) at 4°C for 24 - 48 hours. The biocytin-filled neurons were subsequently visualized using avidin conjugated fluorochrome (Alexa Fluor-647, 1:1000, Invitrogen, UK) in a PB-buffered saline (PBS, 0.9% NaCl) solution containing 3% NGS, 0.1% TritonX-100 and 0.05% NaN_3 for 24 hours at 4°C. Slices were rinsed in PBS and then desalted in PB before being mounted in on glass slides (Fluoromount-G, Southern Biotech) with a 300 µm thick metal spacer, cover-slipped and sealed. Visualized neurons were imaged on a laser scanning confocal microscope (FV1000, Olympus, Japan) for morphological identification. Selected neurons were reconstructed from composite image-stacks obtained with a 30x silicone immersion lens (N.A. 1.05, UPlanSApo, Olympus) over the whole extent of the cells.

Data analysis and visualisation

Intrinsic Physiology Feature Analysis

Recent large-scale studies have demonstrated the necessity of automated analysis (*12, 29*). Comparable to their approaches, we built an analysis pipeline consisting of custom Matlab scripts (MathWorks). Following experiments, the raw membrane voltage traces from both setups were imported into Matlab and a database was populated by automatically extracting parameters from the raw traces and incorporating metadata from experiment documentation. For each neuron 15 active and passive electrophysiological properties were automatically extracted (Supp. Fig. 1).

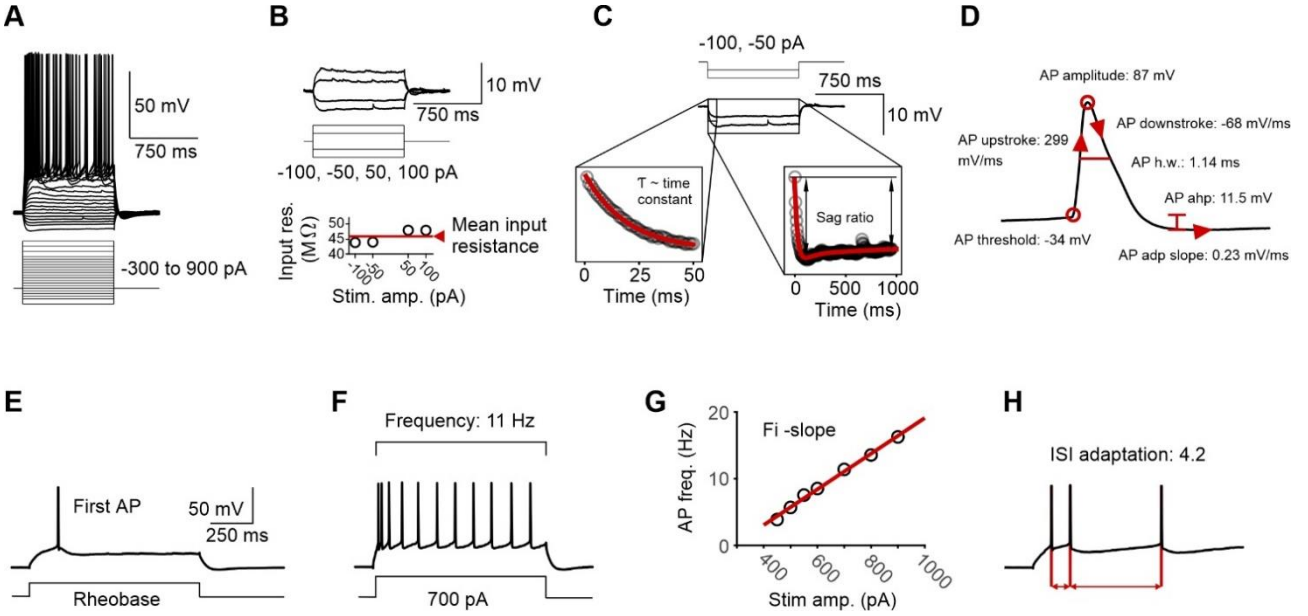

Supplementary figure 1: Extraction of passive and active electrophysiological parameters from current clamp traces shown for one example neuron. (A) Stimulation paradigm consists of increasing step current injections (-300 to 900 pA; 50 and 100 pA increments). The voltage traces in response to the stimulation are shown. **(B)** The displayed voltage responses to the –100, –50, 50 and 100 pA steps are used to calculate the input resistance as the difference between the steady state voltage and the resting membrane potential, divided by the injected current. The bottom graph shows input resistance in relation to step current amplitude, as well as the mean of the four values, which is taken as the final input resistance. **(C)** Magnification of voltage traces, superimposed by the curves (red lines), that were fit to the voltage traces to obtain the membrane time constant and sag ratio (see Methods). **(D)** First action potential (AP) elicited by the example neuron. The AP threshold and peak are marked by red circles, the difference between them is the AP amplitude. The AP upstroke, downstroke and afterdepolarization slope (AP adp slope) are indicated by arrowheads, the half-width (AP h.w.) and afterhyperpolarization (AP ahp) are indicated by lines. **(E)** The step current injection, that elicits the first AP is referred to as rheobase. **(F)** Frequency of AP's, fired in response to 700 pA step current, is defined as the firing frequency. **(G)** Scatterplot showing the firing frequency in relation to the amplitude of the step current injection. The slope of the red line, which is a linear fit of the data, is the frequency/current-slope (Fi-slope). **(H)** Schematic of inter-spike interval adaptation (ISI adaptation) calculated as the ratio of the second inter-spike interval to the first inter-spike interval (5 ratios were calculated from different step current responses and the mean was taken as the final value, see Methods).

Resting membrane potential, input resistance, membrane time constant and sag ratio:

To estimate the *resting membrane potential,* the average amplitudes of four 150 ms trace segments, located before the –50, 50, 100 and 150 pA step current injections, were calculated. The mean of the four values was used as the final *resting membrane potential*. The *input resistance* was calculated as the difference between the steady state voltage and the *resting membrane potential*, divided by the injected current, using –100, –50, 50, 100 pA current steps. The average voltage of the last 100 ms before the end of the step current stimulus was defined as the steady state (*12*). The mean of the *input resistance* values at the different step current injections was used as the final *input resistance* (Supp. Fig. 1B). To estimate the *membrane time constant*, the τ-values of mono-exponential functions (1), which were fit to the initial segments of the voltage responses to the –50 and –100 pA step currents, were utilized. We used the mean of the two τ values as the *membrane time constant* (Supp. Fig. 1C).

$$(1)\quad ae^{\frac{-x}{\tau}} + b$$

To approximate the sag, we fit the voltage response to a –100 pA step current with a function of the form (2). The sag ratio was calculated from the model fit as the ratio of the negative peak voltage amplitude measured from resting membrane potential and the respective amplitude of the steady state voltage during current injection (Supp. Fig. 1C).

$$e^{\frac{-(x-c)}{\tau_1}} - \left(ae^{\frac{-(x-c)}{\tau_2}} + be^{\frac{-(x-c)}{\tau_3}} \right) - d \quad (2)$$

De-filtering of action potential traces:

Action potentials (AP) are fast signals and thus prone to filtering artifacts. Since it is not possible to compensate the entire capacitance of the patch-clamp pipette in current clamp mode, its remainder (referred to as parasitic capacitance; (*43*)), combined with the access resistance, form a filter. Some AP parameters extracted from the original traces show a correlation with the access resistance due to an increasing effect of this filter with larger access resistance (Supp. Fig. 2C-J). The AP upstroke and the AP amplitude are affected the most (Pearson correlation coefficient is –0.59 for both correlations). Even if one sets strict limits for the access resistance of included recordings, this filter artifact will still affect AP shape parameters recorded with low access resistance. Since we measured the access resistance, and can estimate the parasitic capacitance, we can hence approximate the effect of the filtering. In an approach similar to that of Jayant et al. (*44*) we used an inverse digital RC-filter algorithm to produce a de-filtered AP signal for each neuron. Supplemental figure 2 shows a comparison between the original and the de-filtered AP signals (Supp. Fig. 2A-B). The parameters extracted from the de-filtered signals show a much weaker correlation with the access resistance (Supp. Fig. 2C-J). Correcting for the dependence of parameters on the access resistance allowed further analysis with minimized technical bias.

Action potential parameters:

AP parameters were extracted from the first AP elicited in response to a series of increasing step current injections (increments of 50 pA) (Supp. Fig. 1D). All measurements were taken from the de-filtered trace. The *AP threshold amplitude* was measured on the ascending trace where the slope exceeded 20 mV/ms. The maximum and the minimum of the AP slope were defined as the *AP upstroke* and *downstroke*, respectively. The *AP amplitude* was measured from the *AP threshold* to the maximum peak. The *AP halfwidth* is the width of the AP in milliseconds at half amplitude. The *AP afterhyperpolarization* was measured as the difference between the *AP threshold* and the minimum after the AP. If no minimum was reached in a 10.0 ms time window, then the amplitude at the point after the AP, where the slope exceeded –0.2 mV/ms was used instead. The *AP afterdepolarization slope* was defined as the mean slope of the voltage trace in a 1.0 ms time window after the *AP afterhyperpolarization*.

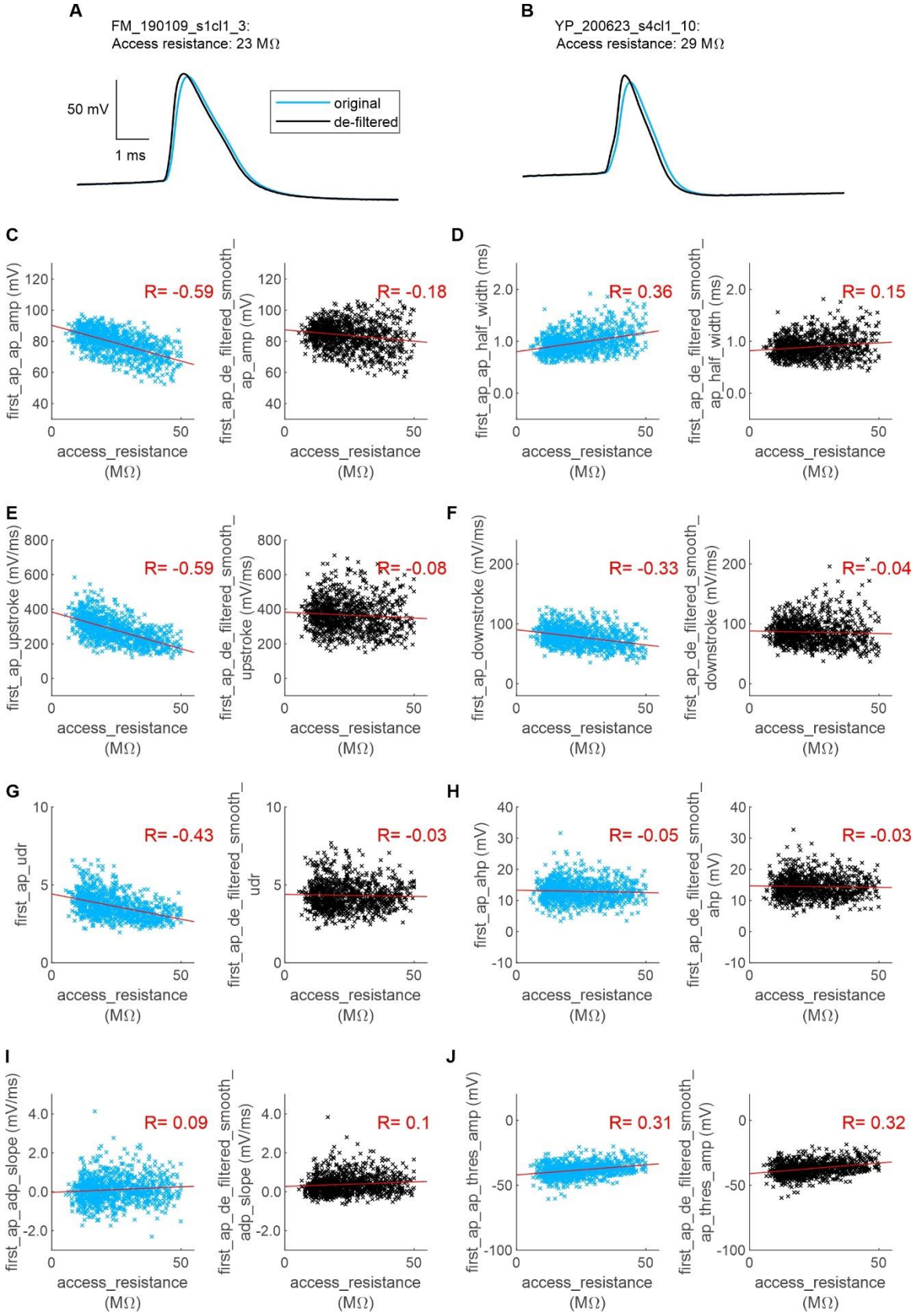

Supplemental figure 2. De-filtering of action potential traces. A-B Two example recordings are shown. The original AP trace (blue) was de-filtered (black AP trace) using an inverse digital RC-filter algorithm. The access resistance and an estimated parasitic capacitance of 4.5 pF were used to construct the inverse filter. Note that the de-filtered APs are faster and larger. **C-J** The different AP parameters of all 964 included pyramidal neurons are plotted against the access resistance. Values derived from the original trace are shown in blue, the values from the de-filtered trace are shown in black. Red lines are least square lines and red numbers indicate the Pearson correlation coefficient. Note that the de-filtering reduces the effect of access resistance on the data, which are present even for recordings with low access resistance.

Firing properties:

To characterize the firing properties of a neuron, the *rheobase*, *firing frequency*, *frequency/current slope (Fi slope)* and the *interspike interval adaptation index (ISI adaptation)* were extracted. The first step current stimulus that elicited at least one AP is referred to as the *rheobase* (Supp. Fig. 1E). The *firing frequency* is the frequency of APs elicited in response to a 700 pA step (Supp. Fig. 1F). The *fi slope* is the slope of a linear fit through the firing frequencies at increasing step current amplitudes (50-100 pA increments) (Supp. Fig. 1G). To calculate the *ISI adaptation* the first five step currents that elicited at least three APs were used (*12*). The *ISI adaptation* was calculated separately for each current injection by dividing the second inter-spike interval (interval between second and third AP) by the first (interval between the first and second AP) (Supp. Fig. 1H). The mean value of those five ratios was calculated for the final *ISI adaptation* (if less than five values were available, the mean of all available values was calculated).

Quality control:

To exclude unhealthy neurons and suboptimal recording conditions, we only included neurons for further analysis when they met the following criteria:

- Resting membrane potential between -90 mV and -60 mV (without liquid junction potential correction)
- Access resistance < 50 MΩ (mean: 24 MΩ, SD: 10 MΩ).

Of 1429 patch-clamp recordings, 1007 neurons met the inclusion criteria. For 979 of these neurons, all 15 electrophysiological properties could be extracted. 15 neurons were labelled as interneurons based on an initial hierarchical clustering. The remaining 964 pyramidal neurons were included for the study.

Statistical analysis

Statistical analyses and data visualisation were performed using R (*45*) and the IDE RStudio (*46*). Unless otherwise specified, the 'tidyverse' R package was utilized to graph the data (*47*). The R packages used for statistical analyses are cited in the respective sections below.

Parameter distribution, correlation and principal component analysis

The measures of central tendency (median) and dispersion (interquartile range) of the 15 active and passive electrophysiological properties were analysed using the 'base' and 'stats' packages of R (*45*). The skewness, kurtosis and related parameters were calculated using the 'moments' package (*48*). The correlation matrix containing Pearson correlation coefficients of the 15 electrophysiological properties was calculated using the 'stats' package and visualized using the 'ggcorrplot' package (*49*). The principal component analysis (PCA) of the 15 electrophysiological properties was performed using the 'prcomp' function of the 'stats' package. Before performing PCA, the data was standardized (z-scores).

Unsupervised hierarchical clustering analysis

We performed a hierarchical clustering analysis of all included neurons with complete data (n = 979) based on the 15 electrophysiological properties, using the 'hclust' function of the 'stats' package. Prior to clustering, the data was standardized (z-scores). Euclidian distance between data points was calculated and 'ward.D2' linkage criterion was used as the agglomeration method (*50*). The resulting dendrogram was cut at the level of two groups. One of the two resulting groups contained 15 neurons with clear interneuron characteristics upon manual inspection. These neurons were removed from the subsequent analysis. The remaining 964 pyramidal neurons were clustered again using the same approach (Euclidean distance and 'ward.D2' method). The 'sigclust2' package was used to test the statistical significance of the hierarchical clustering using a Monte Carlo based approach (*30*). The significance level was set to alpha = 0.05 and the minimum number of neurons that needed to be

present below a given bifurcation of the dendrogram for the algorithm to continue to calculate a p-value was set to 125 (approximately one eighth of the dataset). This procedure yielded seven statistically significant pyramidal neuron groups. We merged the last three groups that were separated in the hierarchical order of the dendrogram, because of their similarity with respect to most parameters except for the *resting membrane potential* and associated parameters. These three groups therefore may correspond to the same functional subtype recorded at different membrane voltages. In total, this procedure yielded five clusters of pyramidal neurons that differed significantly in their electrophysiological properties.

UMAP visualisation

To visualize our 15-dimensional parameter space (15 electrophysiological properties), we used the Uniform Manifold Approximation and Projection (UMAP) technique for dimensionality reduction ('umap' package, (*51, 52*). The data was standardized (z-score) before performing dimensionality reduction. The UMAP figures were plotted using the following hyperparameters: n_neighbors = 60, spread = 0.15, min_dist = 0.001. To generate patient-specific UMAP plots, the coordinates of the UMAP projection of the pooled data were used, but only patient specific data points were displayed.

Random Forest Feature Importance

The most distinguishing electrophysiological property for each neuron subtype was identified using a Random Forest approach. Our labelled data (e-type labels) was used to generate a Random Forest decision tree ensemble using the 'randomForest' package (*53*). As a measure of feature importance, the mean decrease of the Gini index from splitting on a certain property, was extracted for each neuron subtype in comparison to the other subtypes. The property with the largest mean decrease of the Gini index was interpreted as the most distinguishing one for a certain subtype.

Linear mixed-effects modelling

Linear mixed-effects models were fit to the data using the 'lme4' package (*54*). For each electrophysiological property, we modeled patient identity and e-type as random intercepts and the cortical depth as fixed intercept and slope: '*electrophysiological parameter ~ cortical depth + (1|patient identity) + (1|e-type)*'. The fractions of variance explained by cortical depth (corresponding to marginal R^2), e-type and patient identity were calculated from the respective models using the 'insight' package (*55*). The residual variance represents the unexplained variance (residual variance = 1 – conditional R^2) that is independent of the predictors in these models.

References

1. S. Ramón y Cajal, *Textura del SistemaNervioso del Hombre y de los Vertebrados.*, (Moya, Madrid, Spain., 1899/1904).
2. H. Markram *et al.*, Interneurons of the neocortical inhibitory system. *Nature Reviews Neuroscience* **5**, 793-807 (2004).
3. Z. Molnár, A. F. P. Cheung, Towards the classification of subpopulations of layer V pyramidal projection neurons. *Neuroscience Research* **55**, 105-115 (2006).
4. J. DeFelipe *et al.*, New insights into the classification and nomenclature of cortical GABAergic interneurons. *Nature Reviews Neuroscience* **14**, 202-216 (2013).
5. J. Berg *et al.*, Human neocortical expansion involves glutamatergic neuron diversification. *Nature* **598**, 151-158 (2021).
6. N. W. Gouwens *et al.*, Classification of electrophysiological and morphological neuron types in the mouse visual cortex. *Nature Neuroscience* **22**, 1182-1195 (2019).
7. B. I. C. C. Network *et al.*, A multimodal cell census and atlas of the mammalian primary motor cortex. *Nature* **598**, 86-102 (2021).
8. R. D. Hodge *et al.*, Conserved cell types with divergent features in human versus mouse cortex. *Nature* **573**, 61-68 (2019).
9. Z. Yao *et al.*, A transcriptomic and epigenomic cell atlas of the mouse primary motor cortex. *Nature* **598**, 103-110 (2021).
10. Z. Yao *et al.*, A taxonomy of transcriptomic cell types across the isocortex and hippocampal formation. *Cell*, (2021).
11. B. Tasic *et al.*, Shared and distinct transcriptomic cell types across neocortical areas. *Nature* **563**, 72-78 (2018).
12. F. Scala *et al.*, Phenotypic variation of transcriptomic cell types in mouse motor cortex. *Nature* **598**, 144-150 (2021).
13. H. Zeng, J. R. Sanes, Neuronal cell-type classification: challenges, opportunities and the path forward. *Nature Reviews Neuroscience* **18**, 530-546 (2017).
14. T. E. Bakken *et al.*, Comparative cellular analysis of motor cortex in human, marmoset and mouse. *Nature* **598**, 111-119 (2021).
15. J. Lourenço, A. Bacci, Human-Specific Cortical Synaptic Connections and Their Plasticity: Is That What Makes Us Human? *PLOS Biology* **15**, e2001378 (2017).
16. R. S. Hill, C. A. Walsh, Molecular insights into human brain evolution. *Nature* **437**, 64-67 (2005).
17. M. Marín-Padilla, Ontogenesis of the pyramidal cell of the mammalian neocortex and developmental cytoarchitectonics: A unifying theory. *Journal of Comparative Neurology* **321**, 223-240 (1992).
18. A. Gidon *et al.*, Dendritic action potentials and computation in human layer 2/3 cortical neurons. *Science* **367**, 83-87 (2020).
19. L. Beaulieu-Laroche *et al.*, Enhanced Dendritic Compartmentalization in Human Cortical Neurons. *Cell* **175**, 643-651.e614 (2018).
20. H. Mohan *et al.*, Dendritic and Axonal Architecture of Individual Pyramidal Neurons across Layers of Adult Human Neocortex. *Cerebral Cortex* **25**, 4839-4853 (2015).
21. H. M. Chameh *et al.*, Diversity amongst human cortical pyramidal neurons revealed via their sag currents and frequency preferences. *Nature Communications* **12**, 2497 (2021).
22. B. E. Kalmbach *et al.*, h-Channels Contribute to Divergent Intrinsic Membrane Properties of Supragranular Pyramidal Neurons in Human versus Mouse Cerebral Cortex. *Neuron*, (2018).
23. Y. Deitcher *et al.*, Comprehensive Morpho-Electrotonic Analysis Shows 2 Distinct Classes of L2 and L3 Pyramidal Neurons in Human Temporal Cortex. *Cerebral Cortex* **27**, 5398-5414 (2017).
24. B. E. Kalmbach *et al.*, Signature morpho-electric, transcriptomic, and dendritic properties of human layer 5 neocortical pyramidal neurons. *Neuron* **109**, 2914-2927.e2915 (2021).
25. R. Benavides-Piccione, C. Rojo, A. Kastanauskaite, J. DeFelipe, Variation in Pyramidal Cell Morphology Across the Human Anterior Temporal Lobe. *Cerebral Cortex* **31**, bhab034 (2021).
26. H. Pastoll, D. L. Garden, I. Papastathopoulos, G. Sürmeli, M. F. Nolan, Inter-and intra-animal variation in the integrative properties of stellate cells in the medial entorhinal cortex. *eLife* **9**, e52258 (2020).

27. J.-M. Goaillard, A. L. Taylor, D. J. Schulz, E. Marder, Functional consequences of animal-to-animal variation in circuit parameters. *Nature Neuroscience* **12**, 1424-1430 (2009).

28. Y. Peng *et al.*, High-throughput microcircuit analysis of individual human brains through next-generation multineuron patch-clamp. *eLife* **8**, e48178 (2019).

29. S. C. Seeman *et al.*, Sparse recurrent excitatory connectivity in the microcircuit of the adult mouse and human cortex. *eLife* **7**, e37349 (2018).

30. P. K. Kimes, Y. Liu, D. N. Hayes, J. S. Marron, Statistical significance for hierarchical clustering. *Biometrics* **73**, 811-821 (2017).

31. H. M. Chameh *et al.*, Sag currents are a major contributor to human pyramidal cell intrinsic differences across cortical layers. *bioRxiv*, 748988 (2020).

32. S. Weiler *et al.*, Functional and structural features of L2/3 pyramidal cells continuously covary with pial depth in mouse visual cortex.

33. A. V. Zaitsev, N. V. Povysheva, G. Gonzalez-Burgos, D. A. Lewis, Electrophysiological classes of layer 2/3 pyramidal cells in monkey prefrontal cortex. *Journal of Neurophysiology* **108**, 595-609 (2012).

34. K. I. v. Aerde, D. Feldmeyer, Morphological and Physiological Characterization of Pyramidal Neuron Subtypes in Rat Medial Prefrontal Cortex. *Cerebral Cortex* **25**, 788-805 (2015).

35. Y. Ueta *et al.*, Ipsi- and contralateral corticocortical projection-dependent subcircuits in layer 2 of the rat frontal cortex. *Journal of Neurophysiology* **122**, 1461-1472 (2019).

36. B. B. Lake *et al.*, Neuronal subtypes and diversity revealed by single-nucleus RNA sequencing of the human brain. *Science* **352**, 1586-1590 (2016).

37. R. Duarte, A. Morrison, Leveraging heterogeneity for neural computation with fading memory in layer 2/3 cortical microcircuits. *PLOS Computational Biology* **15**, e1006781 (2019).

38. N. Perez-Nieves, V. C. H. Leung, P. L. Dragotti, D. F. M. Goodman, Neural heterogeneity promotes robust learning. *Nature Communications* **12**, 5791 (2021).

39. F. Zeldenrust, B. Gutkin, S. Denéve, Efficient and robust coding in heterogeneous recurrent networks. *PLOS Computational Biology* **17**, e1008673 (2021).

40. E. Marder, J.-M. Goaillard, Variability, compensation and homeostasis in neuron and network function. *Nature Reviews Neuroscience* **7**, 563-574 (2006).

41. N. A. Goriounova *et al.*, Large and fast human pyramidal neurons associate with intelligence. *eLife* **7**, e41714 (2018).

42. A. Guet-McCreight *et al.*, Age-dependent increased sag current in human pyramidal neurons dampens baseline cortical activity.

43. B. Barbour. (https://www.biologie.ens.fr/~barbour/, 2014).

44. K. Jayant *et al.*, Flexible Nanopipettes for Minimally Invasive Intracellular Electrophysiology In Vivo. *Cell Reports* **26**, 266-278.e265 (2019).

45. R Core Team. (R Foundation for Statistical Computing, Vienna, 2021).

46. RStudio Team. (RStudio, PBC, Boston, MA, 2021).

47. H. Wickham *et al.*, Welcome to the Tidyverse. *Journal of Open Source Software* **4**, 1686.

48. L. Komsta, F. Novomestky (2015). moments: Moments, cumulants, skewness, kurtosis and related tests. R package version 0.14.

49. Kassambara, A. (2019). ggcorrplot: Visualization of a Correlation Matrix using 'ggplot2'. R package version 0.1.3.

50. F. Murtagh, P. Legendre, Ward's Hierarchical Agglomerative Clustering Method: Which Algorithms Implement Ward's Criterion? *Journal of Classification* **31**, 274-295 (2014).

51. L. McInnes, J. Healy, J. Melville, UMAP: Uniform Manifold Approximation and Projection for Dimension Reduction. *arXiv*, (2018).

52. T. Konopka (2020). umap: Uniform Manifold Approximation and Projection. R package version 0.2.7.0.

53. A. Liaw, M. Wiener, Classification and Regression by RandomForest. *Forest* **23**, (2001).

54. D. Bates, M. Mächler, B. Bolker, S. Walker, Fitting Linear Mixed-Effects Models Using lme4. *Journal of Statistical Software* **67**, 1 - 48 (2015).

55. D. Lüdecke, P. Waggoner, D. Makowski, Insight: A unified interface to access information from model objects in R. *Journal of Open Source Software* **4**, 1412.